Green-Synthesized FeNPs Driving SDG 6: A Dual-Functional Catalyst for Rapid Dye Degradation and Antibacterial Action

Deeksha Shekhawat
Uttaranchal University
Sanjana Tewari
IFTM: IFTM University
Mitali Panchpuri
DIT-Faculty of Pharmacy: DIT University Faculty of Pharmacy
Dheeraj Koranga
Uttaranchal University
Ritu Painuli
ritsjune8.h@gmail.com
Uttaranchal University

Research Article

Keywords: Green, SDG 6, photocatalysts, dyes, kinetics, antibacterial, wastewater remediation

Posted Date: December 22nd, 2025

DOI: https://doi.org/10.21203/rs.3.rs-8266490/v1

Version of Record: A version of this preprint was published at Environmental Science and Pollution Research on April 5th, 2026. See the published version at https://doi.org/10.1007/s11356-026-37721-z.

Abstract

The green synthesis of iron nanoparticles (FeNPs) by *Crassula ovata* (CO) extract and their photocatalytic degradation of Methyl Orange (MO) dye has been described in this study. The formation of nanoparticles was ensured by UV–Visible spectroscopy with a distinct peak at 261 nm.. The EDX asserted the existence of C, O, Cl, K, Ca, and Fe. XRD analysis established the polycrystalline nature of FeNPs, with both metallic α-Fe and magnetite (Fe_3O_4) phases, which indicated a core–shell structure. Photocatalytic experiments revealed 94% dye degradation of MO within 50 minutes in the presence of sunlight. Kinetic experiments revealed that the pseudo-second-order model fits best in the adsorption process (R^2=0.996). Scavenger experiments revealed hydroxyl radicals, superoxide ions, and electrons as predominant reactive species in dye degradation, with negligible contribution from holes. Reusability experiments proved the stability of the catalyst, which retained 90% activity after five cycles. In addition to photocatalytic performance, the synthesized FeNPs exhibited promising antibacterial activity against both *Escherichia coli*and *Staphylococcus aureus*. Importantly, this work directly aligns with Sustainable Development Goal 6 (Clean Water and Sanitation) by offering an eco-friendly and effective solution for wastewater purification and microbial control.

1. Introduction

The world is becoming more concerned about the environmental safety due to the growing usage of organic, inorganic chemicals in many industrial and agricultural activities (Painuli 2020). The natural environment is enormously harmed by the hazardous and uncontrollable organic, inorganic pollutants found in wastewater from industries including paper and pulp, chemicals, petrochemicals, dyeing, etc. (Painuli 2020). Several organic dyes and their intermediates are continuously utilized in the paint, textile, plastic, ink, and cosmetics industries. Dyes are among the several organic contaminants that are often employed and released into the aquatic environment (Chaudhary 2024). Water pollution from dangerous synthetic dyes has become a major global concern due to the printing, leather, and textile industries rapid rise. Due to their great persistence, carcinogenicity, and resistance to conventional wastewater treatment methods, these dye pollutants represent serious risks to human health and aquatic ecosystems. Ensuring the removal of such contaminants is essential to achieving Sustainable Development Goal 6 (SDG 6): Clean Water and Sanitation, which emphasises improving water quality by reducing pollution, minimising the release of hazardous chemicals, and promoting safe and affordable wastewater treatment technologies. In this sense, enhanced photocatalytic degradation using environmentally friendly metal oxide nanoparticles offers a practical and sustainable solution to dye contamination and directly contributes to the worldwide goal for clean and safe water (Baby 2023,Castillo-Suárez 2023). Colors are essential to our daily existence and are employed in practically every manufacturing area of the economy. During the textile runoff dyeing operations, around 15% of the total dyes generated worldwide are wasted. Apart from exacerbating the issue of color in aquatic environments, the textile and color industries' color effluents also endanger aquatic life by diminishing or even stopping the water's capacity to replenish its oxygen supply through photosynthesis (Aaga 2023). In addition to these, variety of dyes find their way into drinking water, posing a major risk to human health

because some of them are carcinogenic (Sharma 2018). The environmental issue of wastewater and its toxicity is one of the major research topics nowadays. Many studies have been conducted on the environmental and industrial uses of nanomaterials for the identification and deterioration of organic pollutants and dyes. The wastewater from synthetic dyes primarily composed of organic pollutants, which possess complex structure and are extremely difficult to degrade in the natural environment (Al-Tohamy 2022). Anionic azo dyes make up half of the dye synthesis and industrial applications (Chang 2001). Similarly, Methyl orange (MO) is common amnionic azo dye. Azo dyes are among the most concerning organic pollutants because they are widely used in various industries and have developed a resistance to biological and physicochemical treatments, rendering traditional treatment methods ineffective (Bai 2020). It is a water soluble organic synthetic dye give bright orange colour on dissolving in water. Owing to the presence of N = N group in its molecules, they have emerged as carcinogenic, extremely noxious and can cause abnormality in developing foetus during pregnancy (Bai 2020, Haque 2021). Nonetheless, there are methods used for the degradation of these anionic azo dyes into harmless products but they suffer from the complications such as generation of perilous secondary pollutant and toxic sludge. However, each method has several drawbacks, such as a) hazardous by-products that need special handling for removal; b) high temperatures; c) the requirement for substrate or templates, which makes pre-manufacturing and post-removal challenging; and d) pollutants that pose a threat to the environment (Malik 2018, Luo 2016). Therefore, there is an urge to develop effective, economical and environmentally sound methodologies for dyes degradation. Photocatalysis has appeared as an effectual substitute for the degradation of water-soluble dyes and other hazardous organic compounds. In the process, the degradation is processed under the solar light in the presence of efficient photocatalysts (Bopape 2024). Nanoparticles (NPs) have special physicochemical characteristics that allow them to enable more efficient pollutants degradation (Deivayanai 2025). NPs have the potential to be used in a variety of ways, including as medication administration, environmental clean-up, biosensing, separations and analyses of various analyzers, treatments for bacterial, fungal, and parasitic illnesses, imaging, catalysis and many more. Numerous NPs have been successfully employed for dye degradation thus far, including FeNPs, manganese-doped ZnO, zinc ferrite, Au, CdS, $TiO_{2,}$ and zinc ferrite (Mahlaule-Glory 2022). Table 1: shows the comparative data for various catalysts for the degradation of MO dye in sun irradiation. Because of the enhanced surface area, outstanding reactivity, and high photochemical stability, Iron NPs (FeNPs) has appeared as remarkable photocatalyst for azo dye degradation (Weng 2018, Soares 2018). The incredible properties have been showed is due to their large surface to volume ratio. Table 2 represents comparative studies that have been investigated the degradation of the dyes using FeNPs. Although there are numerous physical and chemical method used for the FeNPs synthesis, but they possess boundaries, such as use of toxic chemicals, need of high temperature and pressure and are comparatively expensive (Liu 2017, Khatee 2017, Lam 2018, Zuliani 2017). Therefore, green methods (involving the use of plant materials) came in light for the synthesis of FeNPs. The polyphenolic compounds, flavonoids, alkaloids in the plant extract are utilized for the reduction and stabilization of FeNPs (Zhu 2018).

Owing to the importance of biosynthesis, the present method explores the use of *Crassula ovata* (CO) leaves extract for the synthesis of FeNPs. The polyphenolic compounds in the leaves extract of CO have worked out in the reduction of Fe^{3+} to Fe^{0}, i.e., in the formation as well as stabilization of nanoparticles. Considering the importance of Sustainable Development Goal 6 (Clean Water and Sanitation), the prepared CO@FeNPs have been efficiently used as photocatalyast for the degradation of noxious azo dye, MO under sunlight irradiation. The photocatalyst displayed excellent degradation effectiveness for the dye i.e., 94% for period of 50 min. The effect of parameters like time, equilibrium adsorption isotherms and dosage of photocatalyst was also thoroughly examined to appraise the efficiency of the photocatalyst. Scavenger study revealed $OH^{\cdot}$, $\cdot O_2^{-}$, h^{+} radicals showed a significant role and act as major active for the dye degradation species, whereas electron exhibited minor active species. The kinetics study proves the degradation confirms to the pseudo second-order model and the stability and reusability of CO@FeNPs were also studied. Beyond their photocatalytic efficacy, the synthesized CO@FeNPs also demonstrated notable antibacterial activity against *Escherichia coli* and *Staphylococcus aureus*, with concentration-dependent inhibition zones. The enhanced antimicrobial effect is attributed to the ROS generation and nanoparticle-membrane interactions, which disrupt bacterial integrity.

Table 1
Comparative data for various catalysts in the degradation of MO dye in sun irradiation.

Photocatalyst	Light source	Time (min)	Degradation	Ref.
Fe-doped ZnO	Solar irradiation	90 min	92.1%	(Algarni 2022)
Al/ZnO NPs	UV light irradiation	4 hr	80%	(Peerakiatkhajohn 2021
DL-Fe NPs	Sunlight	-	98.1%	(Yuan 2020)
Ni/ZnO	UV light irradiation	-	94.40%	(Al-Mamun 2023)
Ag–Pd NPs	Sunlight	120 min	67.88%	(Karimi 2022)
Fe NPs	Sunlight irradiation	50 min	94%	Present work

Table 2
Comparative data of reported methods with present methods using iron nanoparticles.

Plant material	Dye	Degradation	Ref.
Henna leaf @FeONPs	Methyl blue	88%	(Abid 2020)
Actinidia chinensis @FeNPs	Alizarin yellow R	93%	(Ahmed 2020)
Carica papaya @ FeNPs	Yellow RR	76.6%	(Bhuiyan 2020)
Ruellia tuberosa @FeONPs	Crystal violet	80%	(Vasantharaj 2019)
Crassula ovata @FeNPs	Methyl orange	94%	Present Work

2. Experimental Section

2.1 Materials and method

Fresh *Crassula ovata* (CO) leaves were purchased from a local nursery in Dehradun, India. Ferric chloride ($FeCl_3$) was procured from Merck Pvt. Ltd. MO dye was received from Sigma-Aldrich. All the glass wares were cleaned with the aqua regia and rinsed with Milli-Q water previous to practice.

2.2 Preparation of plant extract

CO plant leaves were purchased from a local nursery in Dehradun, India. After collecting, the crassula ovata leaves were cleaned with tap water, chopped into fine parts and were dried in an oven. 30 g dried leaves were made into fine powder and placed into a beaker with 250 ml distilled water. The extract was prepared by boiling the powdered leaves at approximately at 40℃ for 4 h. Then the prepared extract was kept for cooling at room temperature, filtered and stored in the refrigerator at 4℃.

2.3 Preparation of CO@Fe NPs

A freshly prepared 0.1 M $FeCl_3$ solution was added to CO leaves extract in 1:2 volume ratio at room temperature. The bio reduction was observed by colour change of the solution from peach to greenish black indicates reduction of Fe^{3+} to Fe^0 i.e., the formation of CO@FeNPs (Fig.1). After that, the resulting solution was completely dried until a black solid precipitate started to formed. The dark precipitate was grinded into a fine powder by scuffing and grinding.

2.4 Photocatalytic degradation

FeNPs synthesized using CO extract were employed to assess the photocatalytic degradation of MO dye. To make a stock solution, 100 milliliters of double-distilled water were mixed with precisely weighed 0.03g of the MO dye. To achieve the satisfactory degradation of dyes using prepared NPs, around 20 ml of CO@FeNPs were added to 50 ml of MO solution and constantly stirred for 30 min. A dye solution devoid of CO@FeNPs was kept as the control. The tubes were subsequently exposed to sun irradiation in order to enable the photocatalytic breakdown of the dye. To verify that the MO had completely degraded, the suspension mixture's absorption spectra was routinely examined with a UV–vis spectrophotometer. The given equation was then used to evaluate the percent dye degradation:

$$\% \text{ Degradation} = C_i\text{-}C_0/C_i \times 100$$

Where, **Ci and Cf** are the dye's initial and final concentrations, respectively.

$$\text{Adsorption Capacity(qe)} = (C_0 - Ce) \times V/m$$

Where, **Ce** = Initial MO concentration (mg L^{-1}); $\mathbf{C_0}$ = Equilibrium MO) concentration (mg L^{-1}); **qe** = MO adsorbed at equilibrium (mg g^{-1}); **V** = Volume of the solution (L)

2.5 Antibacterial study

The antibacterial activity of the CO@FeNPs extract was evaluated against *Staphylococcus aureus* (ATCC 6538) and *Escherichia coli* (ATCC 8739) using the agar well diffusion method. The bacterial strains were obtained from the Microbial Type Culture Collection (MTCC), Chandigarh, India. The assay was performed by introducing the test samples into wells punched into agar plates previously inoculated with bacterial cultures. The plates were then incubated under suitable conditions, and the antibacterial efficacy was determined by measuring the diameter of the zone of inhibition around each well, indicating the extent of bacterial growth suppression.

3. Results and Discussions

3.1 UV-Vis spectroscopy

Since UV-visible spectroscopy may provide details about a particle's size, shape, stability, and aggregation, it was utilized to look into how nanoparticles originate. The UV-Vis spectrophotometer was used to monitor the synthesis of CO@FeNPs. Consequently, in the UV–visible range, metallic nanoparticles exhibit distinctive optical absorption spectra. Therefore, the nanoparticles synthesis was observed via naked eyes as well by this spectroscopic technique. A well define, sharp peak at 261 nm was observed, confirming the synthesis of nanoparticles (Fig. 2). A separate work that prepared CO@FeNPs from pomegranate peel extract observed similar UV-Vis absorption spectra, with an absorbance peak centred at 261 nm (Jeyasundari 2017).

3.2 SEM and EDX

SEM is used to evaluate the topological properties of the as-obtained CO@Fe-NPs. The Fe NPs pictures, which have an uneven shape, clearly show porosity on their surface (Fig. 3(a)) (Feng 2007). Furthermore, the elemental composition is verified by the use of EDX spectroscopy, as seen in Fig. 3. It shows that the produced nanoparticles have the appropriate elemental composition, which is C, O, Cl, K, Ca, and Fe. Their acquired atomic percentages are shown as 25.9, 35.9, 22.5, 1.6, 2.1, and 11.9% are inset in (Fig. 3

(b)). The active biomolecules in the plant extract employed in the synthesis of CO@FeNPs function as a reductant and stabilizer at the same time (Kuang 2013), which helps to prevent the resulting CO@FeNPs from aggregating.

3.3 XRD

XRD is a crucial technique for analyzing crystal formation and determining the size of the manufactured NPs' crystals. The XRD analysis in (Fig. 4) shows that the synthesis CO@FeNPs indicating that the FeNPs are poly crystalline in nature (Fan 2009). The XRD spectrum showed peaks at 2θ of 16.12, 21.19, 32.14, 37.32, 43.18 and 54.86 which corresponds to diffraction planes of (110), (200), (112), (311), (400), and (422). XRD patterns of the CO@FeNPs show the presence of metallic iron and iron oxide phases, suggesting that the nanoparticles are partially oxidized. The peak at 2θ=43.18° is close to the (110) plane of body-centred cubic (BCC) α-Fe while the peak at 2θ=54.88° corresponds to the (200) plane of α-Fe confirming the existence of the crystalline iron phase. Furthermore, features at 2θ=32° and 2θ=37.32° correspond to the characteristic peaks of magnetite (Fe_3O_4) which develops on FeNPs due to oxidative processes at the particle surfaces. Some low-angle peaks at 2θ=16.12° and 2θ=21.19° do not have standard strong reflections for bulk iron or iron oxides, possibly related to particle impurities, surface effects, or novel structural features in the nanoparticles. An assembly of metallic α-Fe and Fe_3O_4 oxide phases is characteristic of CO@FeNPs and describes their multiple suboxide features at the cost of the metallic iron centre. All the diffraction peaks of the product can be exclusively indexed to a dual-phase composition of the CO@FeNPs, with metallic iron at the core and an oxidized magnetite layer on the surface of JCPDS no. 06-0696 for α-Fe with a lattice parameter, a = 4.9756 A˚, Unit Cell Volume for a cubic cell: V = a = 123.16 A˚.

3.4 FTIR

FT-IR spectra were used to determine which functional groups were present in the produced CO@FeNPs (Fig. 5). It was revealed that the synthesis of CO@FeNPs was caused by several functional groups. The O-H stretching vibrations, or the conversion of Fe^{3+} to Fe^0 caused by polyphenol compounds, are responsible for the absorption intensity band at 3405 cm^{-1}. 1384 cm^{-1} is for asymmetric stretching of CH_3, while the band at 1624 cm^{-1} is caused by aromatic stretching vibrations of C = C. The absorption band about 2908 cm^{-1} shows the vibration of the C-H bond. The existence of C-O and C = C aromatic rings with stretching of O-H bonds is indicated by the peaks at 1,154 and 1,624 cm^{-1}. C-C bending band is represented by the peak at 1540 cm^{-1}. FTIR spectrograph of CO@FeNPs, commonly known as the jade plant, has noticeable peaks related to the different bioactive constituents in its tissues. Broad peak observed at around 3405cm^{-1} usually corresponds to the O-H stretching due to hydroxyl group and this is frequently encountered in water, alcohols and phenolic compounds in plants. Peaks in the range of 2908cm^{-1} are C-H stretching peaks due to the presence of alkanes in fatty acids and lipids. The band 1773cm^{-1} is usually associated with C = O stretch which is common for carbonyl functional group found in esters, aldehydes, ketones and even acids. Likewise, as in the case of aromatic rings may generate

stretching peaks between 1624cm^{-1} due to C = C stretch motion. C-O stretching vibration of ethers, esters or alcohols will have peaks in the region around 1154cm^{-1}, and the fingerprint region (690 cm^{-1}) contributes unique bending modes that may potentially enable differentiation of components present in *Crassula ovata* leaves extract (Abodunrin 2015).

3.5. Photocatalytic degradation of dye

3.5.1 Effect of Time on the Photocatalytic Degradation

CO@FeNPs were allowed to degrade aqueous solutions containing 1mM MO dye at variable time interval. Photographs provide visual depictions of the dilution and catalytic action of MO during its degradation process. The photos depict the progression of MO's appearance across various periods, ranging from 0 to 50 minutes. When the deterioration process first begins (0 min), the photographic image has a rich, deep red color that is typical of the untreated MO dye. As the process of deterioration progresses, a discernible shift takes place. Following these time intervals of 10, 20, 30, 40, and 50 minutes, there is a noticeable shift in the dye's colour. The MO dye's colour gradually changes over time, going from a darker, more intense shade to a lighter shade. The color shifts from bright concentrated to softer more subdued tone indicated that MO has been positively broken into smaller molecular components (Fig. 6 (a)). (Umamaheswari 2018).

With increasing irradiation intervals, the photodegradation of the MO dye progressively intensifies. The intensity of SPR peak decreases as a function of time increases. Based on the corresponding strength of the UV–vis spectral peak, the degradation of MO was assessed (Fig. 6 (b)). The MO dye's % degradation is depicted in Fig. 6 (b). The graph clearly depicts that the percentage of degradation increases with the length of solar irradiation.

At 10, 20, 30, 40, and 50 minutes, respectively, the dye showed degradation rates of 36%, 47%, 63%, 78%, and 94%. This UV-visible graph essentially provides visual indication of the photocatalytic degradation process. The steady and uniform disintegration of MO dye molecules is established by the progress in the degradation percentage over higher radiation durations. This graph provides an information of the degradation kinetics, illustrating the relationship between the length of time exposed to sunlight and the efficiency of dye degradation (Salam 2019).

Kinetics of adsorption was modelled by Pseudo first order and Pseudo second order kinetics which are represented by Eqs. 1 and 2 respectively.

$\log (q_e - q_t) = \log q_e - \frac{k1}{2.303t}$ (1)

$$\frac{t}{D_t} = \frac{1}{k_2 D_e^2} + \frac{t}{D_e}$$

Where qe and qt are the amount (mg/g) of MO dye adsorbed on CO@FeNPs at equilibrium and specified time intervals, t(min) respectively; k_1 and k_2 are the rate constants of the pseudo first-order and pseudo-second-order models, respectively. Linear plots of both these models are presented Fig. 6 (a) and (b). MO removal studies were carried out with CO@FeNPs using a time-dependent removal analysis and kinetic modelling. Rapid increase of MO removal occurred within 40 min, then around 50 min reached the equilibrium point. Kinetic studies were done by using pseudo-first-order and pseudo-second-order models. The pseudo-first-order model was well correlated with an (R^2) value of 0.9867; however, the pseudo-second-order model offered a better fit with an (R^2) value of 0.996 (Fig. 6 (c & d). This implies that the adsorption mechanism is better described by the pseudo-second-order model, implying that chemisorption dominates the interaction between MO and CO@FeNPs (Yuan 2020)

(b) Time-dependent study of MO by CO@FeNPs, (c) the pseudo-first-order, and (d) the pseudo-second-order

3.5.2 Effect of Dye Concentration on Photocatalytic Degradation

The starting dye concentration was adjusted within the range of 5–25 ml in order to evaluate the effect of the MO dye concentration on the photocatalytic degradation process. The goal of the investigation was to find an appropriate dye concentration throughout the course of 60 minutes while keeping a steady 5 ml of catalyst. As shown in (Fig. 7), the photographic images represent the dilution process that takes place within solutions of MO dye at different concentrations: 5, 10, 15, 20, and 25 ml. These images provide visual representation of how dyes behave after preset 60 minutes degradation period. The images displayed that the change in the dyes initial color and intensity, starts with 5ml dye solution. After the dye concentration is raised to 10 ml, 15 ml, 20 ml, and 25 ml, each photograph shows a more intense and deeper color over time. Over the period of 60 minutes, the degradation process causes color change in the dye solutions'(Rahman 2014). As the dye concentration was increased, (Fig. 7) the degradation rate dropped.

The Beer-Lambert rule states that a high dye concentration shortens the photons' path length upon entry, resulting in less photon adsorption on the catalyst surface and, as a result, reduced photodegradation. Because there are more dye molecules available for excitation and energy transfer at greater starting dye concentrations, the MO dye degrades less quickly as dye concentration rises. Reaction rates are continuous because the surface is not totally covered until the critical threshold is achieved. But over this crucial point, additional increases in the original dye concentration cause the degradation efficiency to significantly decrease for a number of reasons. As the amount of dye rises, more dye molecules are adsorbed on the surface of the photocatalytic material. As a result, the dye molecules absorb more UV light than the nanoparticles do. As a result, light penetration at the photocatalytic surface decreases, which in turn reduces the production of hydroxyl radicals and, ultimately, the effectiveness of dye degradation. Therefore, a greater catalyst surface area is needed when the initial dye concentration rises

in order to produce enough hydroxyl radicals to efficiently attack the accessible dye molecules and enable total dye breakdown (Ramesh 2024).

3.5.3 Equilibrium adsorption isotherms

The Langmuir and Freundlich isotherm models were used to assess the equilibrium adsorption of MO dye onto Crassula ovata@FeNPs to comprehend the mechanism and capacity of the adsorbent prepared. (Fig. 8(a). The Langmuir model, in which monolayer adsorption is predicted on the homogenous surface having finite and similar binding sites, demonstrated a strong fit with the experimental data. The linear graph of 1/qe against 1/Ce shows a high correlation coefficient (R2 = 0.996) wihich confirms that the model is appropriate. The highest monolayer adsorption capacity (Qm) and Langmuir constant (kL) were determined to be 487.80 mg/g and 0.002592 L/mg, respectively, which indicate that *Crassula ovata* @FeNPs have high adsorption capability and high affinity for MO molecules. Freundlich isotherm, which describes adsorption on heterogeneous surfaces, also matched the data fairly well with a correlation coefficient of R^2=0.9815. The Freundlich constants KF and 1/n were found to be 2.0905 and 1.2155, respectively. The fact that the value of 1/n is above 1 suggests cooperative adsorption behaviour, which could be the result of interactions between the adsorbed dye molecules at the surface. While both isotherm models showed the adsorption process satisfactorily, however, a better fit was noticed with the Langmuir model, suggesting that the monolayer adsorption is the primary mechanism of MO dye via CO@FeNPs. (Fig. 8 (b & c)) (Table 3).

Table 3
Adsorption isotherms models and their parameter values.

	LangmuirModel			**Freundlich Model**		
Adsorbent	**Q_m(mg/ g)**	**k_L**	**R^2**	**K_F**	**1/n**	**R^2**
CO@FeNPs	487.8049	0.002592	0.995	2.090547	1.215554	0.98036

3.5.4 Scavenger study

EDTA, isopropyl alcohol, benzoquinone and $AgNO_3$ were the four quenchers utilized for determining the role of scavengers that are accountable for the degradation of MO dye. Holes, hydroxy radicals, superoxide and electrons were respectively incorporated in the trapping experiment. The results from the experiment indicated that the degradation rate of the dye remained unaffected after the addition of h^+ (holes) as a quencher. Nonetheless, superoxide and electrons, hydroxy radicals significantly reduced the degradation rate of MO to 28.1, 19 and 17.9 respectively (Fig. 9). Therefore, the most effective responsible for the degradation of dyes are hydroxy radicals followed by the superoxide and electrons. This indicates that when sufficient light was absorbed by the iron surface and it has reached to valence band, the excited electrons also move towards the conduction band leaving holes behind. During this process superoxide and hydroxy radicals are also generated. The electrons as well as the superoxide

radicals that were absorbed at the surface of the material also helped in the elimination of the dye during photocatalytic degradation.

3.5.5 Mechanism for dye degradation

FeNPs large specific surface area and smaller size are known to contribute to their strong adsorption. They also have a reputation for lowering activity and ability. The degradation of dyes is basically related with the generation of electron-hole (e^- & h^+ pair) on the catalyst surface on exposure to sunlight to carry out series of redox reactions. Water molecules on reaction with hole converts into •OH and H^+ ions whereas molecular O_2 converts into O_2•− on reaction with free electrons. The O_2•− then reacts with H_2O to form •OOH radicals (This further rearranged to form H_2O_2). The produced H_2O_2 while reacting with superoxide radical anion transformed to •OH. The generated •OH radical acts as strong oxidising agent that tend to break the azo bond in the dye responsible for color (Emmanuel 2023). The proposed mechanism for the degradation of dye is shown in the following reactions (Scheme 1) and (Scheme 2).

Scheme 2: Pictorial representation showing mechanism for Azo dye degradation

3.5.6. Reusability and Photostability of developed catalyst

The reusability as well as photocatalytic performance of the developed catalyst was crucial to determine the experimental application of developed catalyst. Consequently, the evaluation for the photocatalytic usability and stability have been studied by performing 5 times experiment consequently as seen in Fig. 10. The performance of the developed catalyst was observed to be decreased from 94% to 90% with each cycle for the degradation of anionic azo dye i.e. This decrease in the efficacy could be due to the presence/ adsorption of intermediates on the surface of the developed catalyst. Therefore, the developed photocatalyst displayed excellent reusability and stability for the degradation of MO dye.

3.5.7 Antibacterial activity

FeNPs synthesized via green routes using CO extract have exhibited promising antibacterial activity against both *Escherichia coli* and *Staphylococcus aureus*. The antibacterial efficiency was evaluated using the agar well diffusion method at CO@FeNPs concentrations of 10, 50, and 100 ppm. Results revealed a concentration-dependent increase in the zone of inhibition: for *E. coli*, it was 1.13 ± 0.55 mm (10 ppm), 1.40 ± 0.10 mm (50 ppm), and 1.63 ± 0.11 mm (100 ppm); and for *S. aureus*, 0.68 ± 0.01 mm (10 ppm), 0.92 ± 0.01 mm (50 ppm), and 1.73 ± 0.05 mm (100 ppm) (Fig. 11) and Table 4. These findings suggest that CO@FeNPs effectively suppress bacterial growth, especially at higher concentrations.

The antibacterial mechanism of CO@FeNPs involves their ability to generate reactive oxygen species (ROS), such as hydroxyl radicals (•OH) and superoxide anions (O_2•−), which induce oxidative stress, disrupt the integrity of bacterial cell walls, and damage proteins, lipids, and DNA (Chikkanna 2019). The small particle size and high surface area enhance the interaction between nanoparticles and bacterial membranes, increasing permeability and ultimately leading to cell death (Batool 2021). Moreover, green

synthesis using *Crassula ovata* provides bioactive phytochemicals that serve as natural reducing and stabilizing agents, enhancing the stability and antimicrobial functionality of CO@FeNPs.

Therefore, plant-mediated CO@FeNPs provide an eco-friendly, cost-effective alternative to conventional antibiotics and hold potential for use in biomedical and environmental disinfection applications.

Table 4
Zone of inhibition of CO@FeNPs against *E. coli* and *S. aureus.*

Concentration (ppm)	*E. coli*	*S. aureus*
	CO@FeNPs	CO@FeNPs
10	1.133333 ± 0.55	0.68 ± 0.01
50	1.4 ± 0.1	0.92 ± 0.01
100	1.633333 ± 0.11	1.733333 ± 0.05

3.5.8 Conclusion

The preparation of nanoparticles using biological processes is one of the promising approaches that has received a lot of attention. It generates innovative, environmentally beneficial, and reasonably priced materials with a wide range of applications. The synthesis of FeNPs in this investigation was carried out using a leaves extract solution of Crassula ovata. As a reducing agent as well as stabilizing agent, the plant extract work as an effective plant material. With just 50 minutes of sunlight, 94% of the MO dye could be broken down by the FeNPs' thereby depicting promising photocatalytic activity. Kinetic studies confirmed that the process followed a pseudo-second-order model, indicating chemisorption, and adsorption isotherms showed better agreement with the Langmuir model, revealing high monolayer adsorption capacity (487.80 mg/g). $OH^{\cdot}$, electrons $\cdot O_2^{-}$radicals showed a crucial role and emerged as major active species for the dye degradation in scavenger study. The reusability data for the developed material showed the FeNPs was recyclable and stable upto 5 cycles. Overall, the present study highlights that *Crassula ovata*–mediated FeNPs represent a sustainable, green, and dual-functional nanomaterial with strong potential for integrated wastewater treatment and microbial disinfection. Their ability to efficiently remove organic dyes, combined with significant antimicrobial activity, positions them as promising candidates for real-world environmental remediation. Importantly, this work directly supports Sustainable Development Goal 6 (Clean Water and Sanitation) by contributing to the development of eco-friendly, low-cost, and high-performance materials that can facilitate access to clean water through effective wastewater purification and pollution control.

Declarations

Acknowledgements

The authors would like to thank the Department of Research and Innovation, Uttaranchal University for providing characterization facilities.

Funding

Not Applicable.

Authors contribution

Diksha Chauhan: Data curation, Methodology, **Sanjana Tewari**: Visualization, Data curation, **Mitali Panchpuri**: Investigation, **Dheeraj Koranga:** Data Curation, **Ritu Painuli:** Writing, Reviewing and Editing.

Corresponding author

Ritu Painuli

Ethical approval

Not applicable.

Consent for publication

Not applicable.

Consent to participate

Not applicable.

Competing interests

The authors declare no competing interests.

Data Availability Statement

The data will be available on the reasonable request.

References

1. Aaga, G. F.; Anshebo, S. T.; Green synthesis of highly efficient and stable copper oxide nanoparticles using an aqueous seed extract of Moringa stenopetala for sunlight-assisted catalytic degradation of Congo red and alizarin red s. Heliyon **2023**, 9(5), e16067. doi: 10.1016/J.HELIYON. 2023.E16067.
2. Abid, M. A.; Kadhim, D. A.; Novel comparison of iron oxide nanoparticle preparation by mixing iron chloride with henna leaf extract with and without applied pulsed laser ablation for methylene blue degradation. Journal of Environmental Chemical Engineering **2020**, 8(5), 104138. doi: 10.1016/J.JECE.2020.104138.
3. Abodunrin, T. J.; Obafemi, O.; Boyo, A. O.; Adebayo, T.; Jimoh, R.; The Effect of Electrolyte on Dye Sensitized Solar Cells Using Natural Dye from Mango Leaf as Sensitizer. Advances in Materials Physics and Chemistry **2015**, 05(06), 205–213. doi:10.4236/ampc.2015.56021.

4. Ahmed, A.; Usman, M.; Yu, B.; Ding, X.; Peng, Q.; Shen, Y.; Cong, H.; Efficient photocatalytic degradation of toxic Alizarin yellow R dye from industrial wastewater using biosynthesized Fe nanoparticle and study of factors affecting the degradation rate. Journal of Photochemistry and Photobiology B: Biology **2020**, 202, 111682. doi: 10.1016/J.JPHOTOBIOL.2019.111682.
5. Algarni, T. S.; Abduh, N. A. Y.; Aouissi, A.; Al Kahtani, A.; Photodegradation of methyl orange under solar irradiation on Fe-doped ZnO nanoparticles synthesized using wild olive leaf extract. Green Processing and Synthesis **2022**, 11(1), 895–906. doi:10.1515/gps-2022-0077.
6. Al-Mamun, M. R.; Iqbal Rokon, M. Z.; Rahim, M. A.; Hossain, M. I.; Islam, M. S.; Ali, M. R.; Bacchu, M.S.; Waizumi, H.; Komeda, T.; Khan, M.Z.H.; Enhanced photocatalytic activity of Cu and Ni-doped ZnO nanostructures: A comparative study of methyl orange dye degradation in aqueous solution. Heliyon **2023**, 9(6), e16506. doi: 10.1016/J.HELIYON. 2023.E16506.
7. Al-Tohamy, R.; Ali, S. S.; Li, F.; Okasha, K. M.; Mahmoud, Y. A. G.; Elsamahy, T.; Jiao, H.; Fu, Y.; Sun, J.; A critical review on the treatment of dye-containing wastewater: Ecotoxicological and health concerns of textile dyes and possible remediation approaches for environmental safety. Ecotoxicol. Environmen. Safety **2022**, 231, 113160. doi: 10.1016/J.ECOENV.2021.113160.
8. Baby, M.; Rajeev Kumar, K. Photocatalytic degradation of organic dye under UV light irradiation using hybrid nanostructures. Materials Today: Proceedings **2023**. doi: 10.1016/J.MATPR.2023.03.323.
9. Bai, Y. N.; Wang, X. N.; Zhang, F.; Wu, J.; Zhang, W.; Lu, Y. Z.; Fu, L.; Lau, T.C.;Zeng, R.J.; High-rate anaerobic decolorization of methyl orange from synthetic azo dye wastewater in a methane-based hollow fiber membrane bioreactor. Journ. Hazardous Mater. **2020**, 388, 121753. doi: 10.1016/J.JHAZMAT.2019.121753.
10. Batool, F.; Iqbal, M.S.; Khan, S.D.; Khan, J.; Ahmed, B.; Qadir, M.I.; Biologically synthesized iron nanoparticles (FeNPs) from Phoenix dactylifera have anti-bacterial activities. Sci. Report. **2021** 11 (22132) 1-9. https://doi.org/10.1038/s41598-021-01374-4
11. Bhuiyan, M. S. H.; Miah, M. Y.; Paul, S. C.; Aka, T. Das; Saha, O.; Rahaman, M. M.; Sharif, M.J. S.; Habiba, O.; Ashaduzzaman, M.; Green synthesis of iron oxide nanoparticle using Carica papaya leaf extract: application for photocatalytic degradation of remazol yellow RR dye and antibacterial activity. Heliyon **2020**, 6(8), e04603. doi: 10.1016/J.HELIYON. 2020.E04603.
12. Bopape, D. A.; Ntsendwana, B.; Mabasa, F. D.; Photocatalysis as a pre-discharge treatment to improve the effect of textile dyes on human health: A critical review. Heliyon **2024**, 10(20), e39316. doi: 10.1016/J.HELIYON. 2024.E39316.
13. Castillo-Suárez, L. A.; Sierra-Sánchez, A. G.; Linares-Hernández, I.; Martínez-Miranda, V.; Teutli-Sequeira, E. A.; A critical review of textile industry wastewater: green technologies for the removal of indigo dyes. International Journal of Environmental Science and Technology. Institute for Ionics September 1, 2023, pp 10553–10590. doi:10.1007/s13762-023-04810-2.
14. Chang, J. S.; Lin, C. Y. Decolorization kinetics of a recombinant Escherichia coli strain harboring azo-dye-decolorizing determinants from Rhodococcus sp. Biotechnology Letters **2001**, 23(8), 631–636. doi:10.1023/A:1010306114286.

15. Chaudhary, M.; Kumar, C.; Raghav, S.; Panwar, M.; Pandey, S.; Painuli, R.; Sunlight-driven photocatalytic degradation of industrial dyes using Withania somnifera decorated MnO_2 nanoparticles. Discover Nano **2024**, 19(1). doi:10.1186/s11671-024-04160-z.
16. Chikkanna, M.M.; Neelagund, S.E.; Rajashekarapp, K.K.; Green synthesis of Zinc oxide nanoparticles (ZnO NPs) and their biological activity. SN Applied Sciences **2019,** 1 (117), 1-10 doi:10.1007/s42452-018-0095.
17. Deivayanai, V. C.; Thamarai, P.; Karishma, S.; Saravanan, A.; Vickram, A. S.; Yaashikaa, P. R.; Sonali, S. A comprehensive review on impregnated magnetic nanoparticle in advanced wastewater treatment: An in-depth technical review and future directions.; Sustainable Chemistry for the Environment **2025**, 9, 100220. doi: 10.1016/J.SCENV.2025.100220.
18. Emmanuel, S.S.; Adesibikan, A.A.; Opatola, E.A.; Olawoyin, C.O.; A pragmatic review on photocatalytic degradation of methyl orange dye pollutant using greenly biofunctionalized nanometallic materials: A focus on aquatic body. **2023,** 37,e7108. doi:10.1002/aoc.7108.
19. Fan, J.; Guo, Y.; Wang, J.; Fan, M.; Rapid decolorization of azo dye methyl orange in aqueous solution by nanoscale zerovalent iron particles. Journal of Hazardous Materials **2009**, 166(2–3), 904–910. doi: 10.1016/J.JHAZMAT.2008.11.091.
20. Feng, J.; Lim, T. T.; Iron-mediated reduction rates and pathways of halogenated methanes with nanoscale Pd/Fe: Analysis of linear free energy relationship. Chemosphere **2007**, 66(9), 1765–1774. doi: 10.1016/J.CHEMOSPHERE.2006.06.068.
21. Haque, M. M.; Haque, M. A.; Mosharaf, M. K.; Marcus, P. K.; Decolorization, degradation and detoxification of carcinogenic sulfonated azo dye methyl orange by newly developed biofilm consortia. Saudi Journal of Biological Sciences **2021**, 28(1), 793–804. doi: 10.1016/J.SJBS.2020.11.012.
22. Jeyasundari, J.; Shanmuga Praba, P.; Brightson, Y.; Jacob, A.; Vasantha, V. S.; Shanmugaiah, V.; Chemical Science Review and Letters Green Synthesis and Characterization of Zero Valent Iron Nanoparticles from the Leaf Extract of Psidium Guajava Plant and Their Antibacterial Activity. Chem Sci Rev Lett **2017**, 6(22).
23. Karimi, F.; Rezaei-savadkouhi, N.; Uçar, M.; Aygun, A.; Elhouda Tiri, R. N.; Meydan, I.; Agghapur, E.; Seckin, H.; Berikten, D.; Gur T.; Sen, F.; Efficient green photocatalyst of silver-based palladium nanoparticles for methyle orange photodegradation, investigation of lipid peroxidation inhibition, antimicrobial, and antioxidant activity. Food and Chemical Toxicology **2022**, 169, 113406. doi: 10.1016/J.FCT.2022.113406.
24. Khataee, A.; Kayan, B.; Gholami, P.; Kalderis, D.; Akay, S. Sonocatalytic degradation of an anthraquinone dye using TiO_2-biochar nanocomposite.; Ultrasonics Sonochemistry **2017**, 39, 120–128. doi: 10.1016/J.ULTSONCH.2017.04.018.
25. Kuang, Y.; Wang, Q.; Chen, Z.; Megharaj, M.; Naidu, R. Heterogeneous Fenton-like oxidation of monochlorobenzene using green synthesis of iron nanoparticles.; Journal of Colloid and Interface Science **2013**, 410, 67–73. doi: 10.1016/J.JCIS.2013.08.020.

26. Lam, N. M.; Thi, T. M.; Thanh, P. T.; Yen, N. H.; Dan, N. H.; Structure and magnetic properties of Fe-Co nanoparticles prepared by polyol method. Physica B: Condensed Matter **2018**, 532, 71–75. doi: 10.1016/J.PHYSB.2017.10.039.
27. Liu, J.; He, K.; Wu, W.; Song, T. Bin; Kanatzidis, M. G.; In Situ Synthesis of Highly Dispersed and Ultrafine Metal Nanoparticles from Chalcogels. Journal of the American Chemical Society **2017**, 139(8), 2900–2903. doi:10.1021/jacs.6b13279.
28. Luo, F.; Yang, D.; Chen, Z.; Megharaj, M.; Naidu, R;. One-step green synthesis of bimetallic Fe/Pd nanoparticles used to degrade Orange II. Journal of Hazardous Materials **2016**, 303, 145–153. doi: 10.1016/J.JHAZMAT.2015.10.034.
29. Mahlaule-Glory, L. M.; Mapetla, S.; Makofane, A.; Mathipa, M. M.; Hintsho-Mbita, N. C. Biosynthesis of iron oxide nanoparticles for the degradation of methylene blue dye, sulfisoxazole antibiotic and removal of bacteria from real water. Heliyon **2022**, 8(9). doi: 10.1016/j.heliyon. 2022.e10536.
30. Malik, S. N.; Ghosh, P. C.; Vaidya, A. N.; Mudliar, S. N.; Catalytic ozone pretreatment of complex textile effluent using Fe^{2+} and zero valent iron nanoparticles. Journal of Hazardous Materials **2018**, 357, 363–375. doi: 10.1016/J.JHAZMAT.2018.05.070.
31. Painuli, R.; Joshi, P.; Kumar, D.; Aluminon functionalized silver nanoparticles for the colorimetric detection of aqueous Al(III). Materials Chemistry and Physics **2020**, 239, 122318. doi: 10.1016/J.MATCHEMPHYS.2019.122318.
32. Painuli, R.; Raghav, S.; Jha, P. C.; Athar, M.; Kumar, D. Thermodynamics and kinetics to develop an analytical method for sensing of aqueous Hg(II) using caffeic acid decorated AgNPs. Inorganic and Nano-Metal Chemistry **2023**, 53(3), 239–256. doi:10.1080/24701556.2022.2034012.
33. Peerakiatkhajohn, P.; Butburee, T.; Sul, J. H.; Thaweesak, S.; Yun, J. H.; Efficient and rapid photocatalytic degradation of methyl orange dye using al/zno nanoparticles. Nanomaterials **2021**, 11(4). doi:10.3390/nano11041059.
34. Rahman, N.; Abedin, Z.; Hossain, M. A.; Rapid degradation of azo dyes using nano-scale zero valent iron. American Journal of Environmental Sciences **2014**, 10(2), 157–163. doi:10.3844/ajessp.2014.157.163.
35. Ramesh, N.; Lai, C. W.; Johan, M. R. Bin; Mousavi, S. M.; Badruddin, I. A.; Kumar, A. Sharma, G. Gapsari, F.; Progress in photocatalytic degradation of industrial organic dye by utilising the silver doped titanium dioxide nanocomposite. Heliyon **2024**, 10(24), e40998. doi: 10.1016/J.HELIYON. 2024.E40998.
36. Salam, M. A.; Kosa, S. A.; Al-Nahdi, N. A.; Owija, N. Y.; Removal of Acid Red dye from aqueous solution using zero-valent copper and zero-valent zinc nanoparticles. Desalination and Water Treatment **2019**, 141, 310–320. doi:10.5004/DWT.2019.23303.
37. Sharma, P.; Pant, S.; Rai, S.; Yadav, R. B.; Dave, V.; Green Synthesis of Silver Nanoparticle Capped with Allium cepa and Their Catalytic Reduction of Textile Dyes: An Ecofriendly Approach. Journal of Polymers and the Environment **2018**, 26(5), 1795–1803. doi:10.1007/s10924-017-1081-7.

38. Soares, A.; Ramos, S.; Albergaria, T.; Delerue-Matos, C.; Green zero valent iron nanoparticles dispersion through a sandy column using different injection sequences. Science of The Total Environment **2018**, 637–638, 935–942. doi: 10.1016/J.SCITOTENV.2018.05.096.
39. Umamaheswari, C.; Lakshmanan, A.; Nagarajan, N. S.; Green synthesis, characterization and catalytic degradation studies of gold nanoparticles against congo red and methyl orange. Journal of Photochemistry and Photobiology B: Biology **2018**, 178, 33–39. doi: 10.1016/J.JPHOTOBIOL.2017.10.017.
40. Vasantharaj, S.; Sathiyavimal, S.; Senthilkumar, P.; LewisOscar, F.; Pugazhendhi, A.; Biosynthesis of iron oxide nanoparticles using leaf extract of Ruellia tuberosa: Antimicrobial properties and their applications in photocatalytic degradation. Journal of Photochemistry and Photobiology B: Biology **2019**, 192, 74–82. doi: 10.1016/J.JPHOTOBIOL.2018.12.025
41. Weng, X.; Lin, Z.; Xiao, X.; Li, C.; Chen, Z.; One-step biosynthesis of hybrid reduced graphene oxide/iron-based nanoparticles by eucalyptus extract and its removal of dye. Journal of Cleaner Production **2018**, 203, 22–29. doi: 10.1016/J.JCLEPRO.2018.08.158.
42. Yuan, M.; Fu, X.; Yu, J.; Xu, Y.; Huang, J.; Li, Q.; Sun, D.; Green synthesized iron nanoparticles as highly efficient fenton-like catalyst for degradation of dyes. Chemosphere **2020**, 261, 127618. doi: 10.1016/J.CHEMOSPHERE.2020.127618.
43. Zhu, F.; Ma, S.; Liu, T.; Deng, X.; Green synthesis of nano zero-valent iron/Cu by green tea to remove hexavalent chromium from groundwater. Journal of Cleaner Production **2018**, 174, 184–190. doi: 10.1016/J.JCLEPRO.2017.10.302.
44. Zuliani, A.; Balu, A. M.; Luque, R.; Efficient and Environmentally Friendly Microwave-Assisted Synthesis of Catalytically Active Magnetic Metallic Ni Nanoparticles. ACS Sustainable Chemistry and Engineering **2017**, 5(12), 11584–11587. doi:10.1021/acssuschemeng.7b02945.

Schemes

Schemes 1 and 2 are available in the Supplementary Files section.

Figures

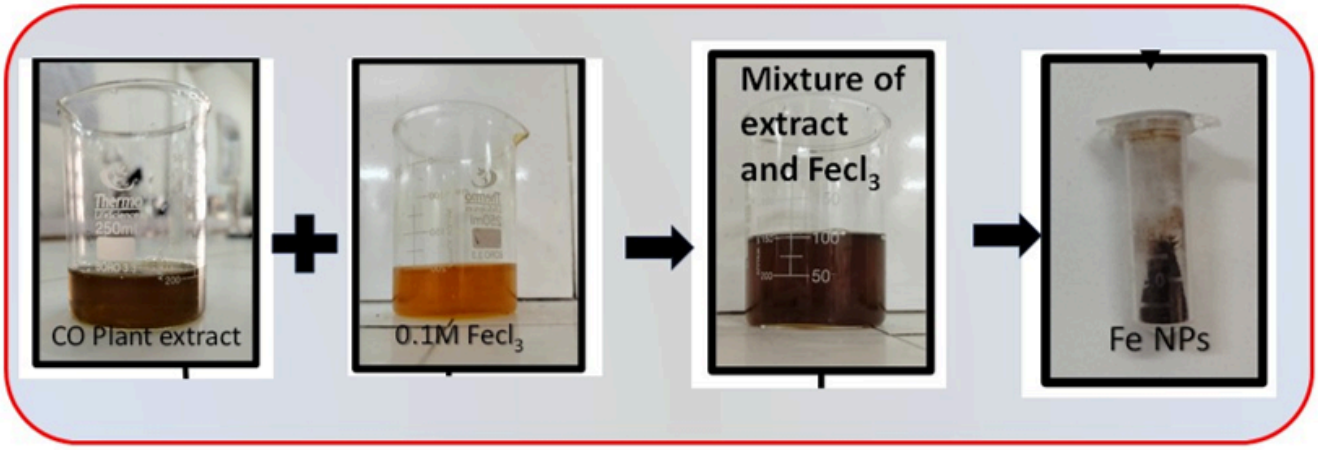

Figure 1

Scheme for the synthesis of CO@FeNPs.

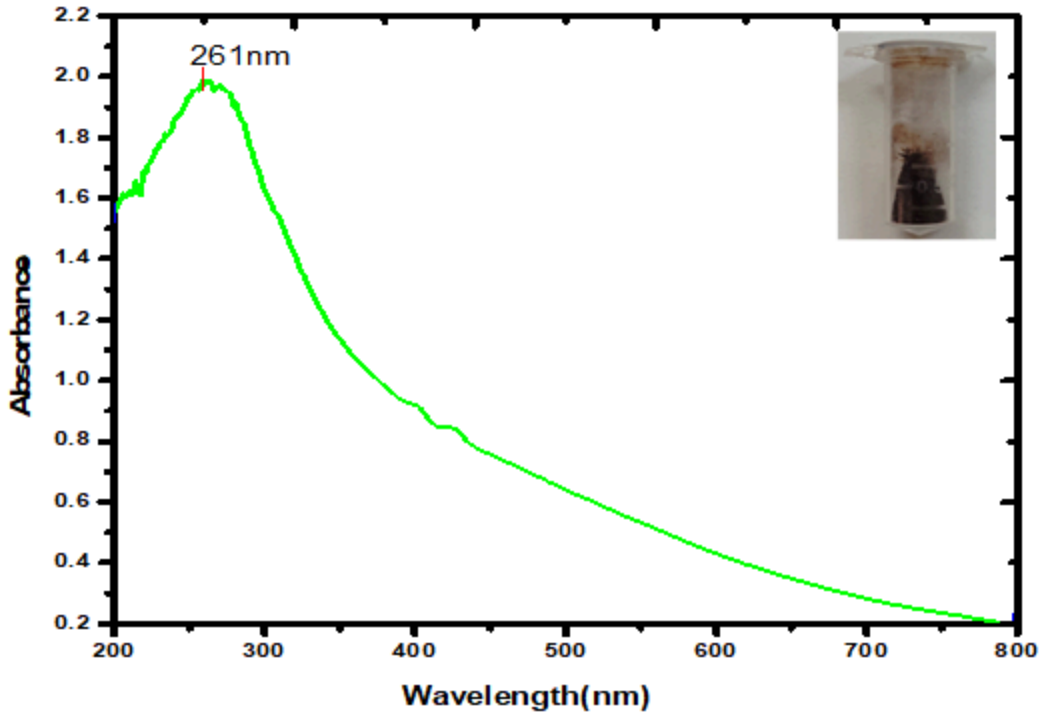

Figure 2

UV-visible spectra of CO@FeNPs (Inset of the image shows the optical image of synthesized NPs)

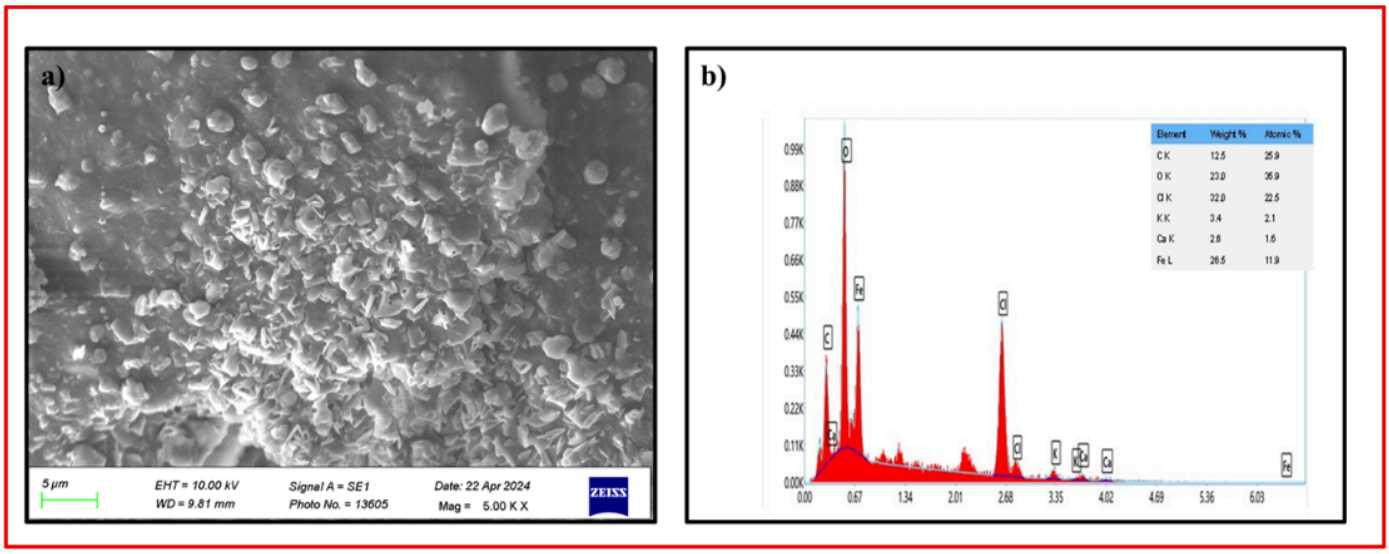

Figure 3

Scanning electron microscopy and EDX Spectrum of synthesised CO@FeNPs

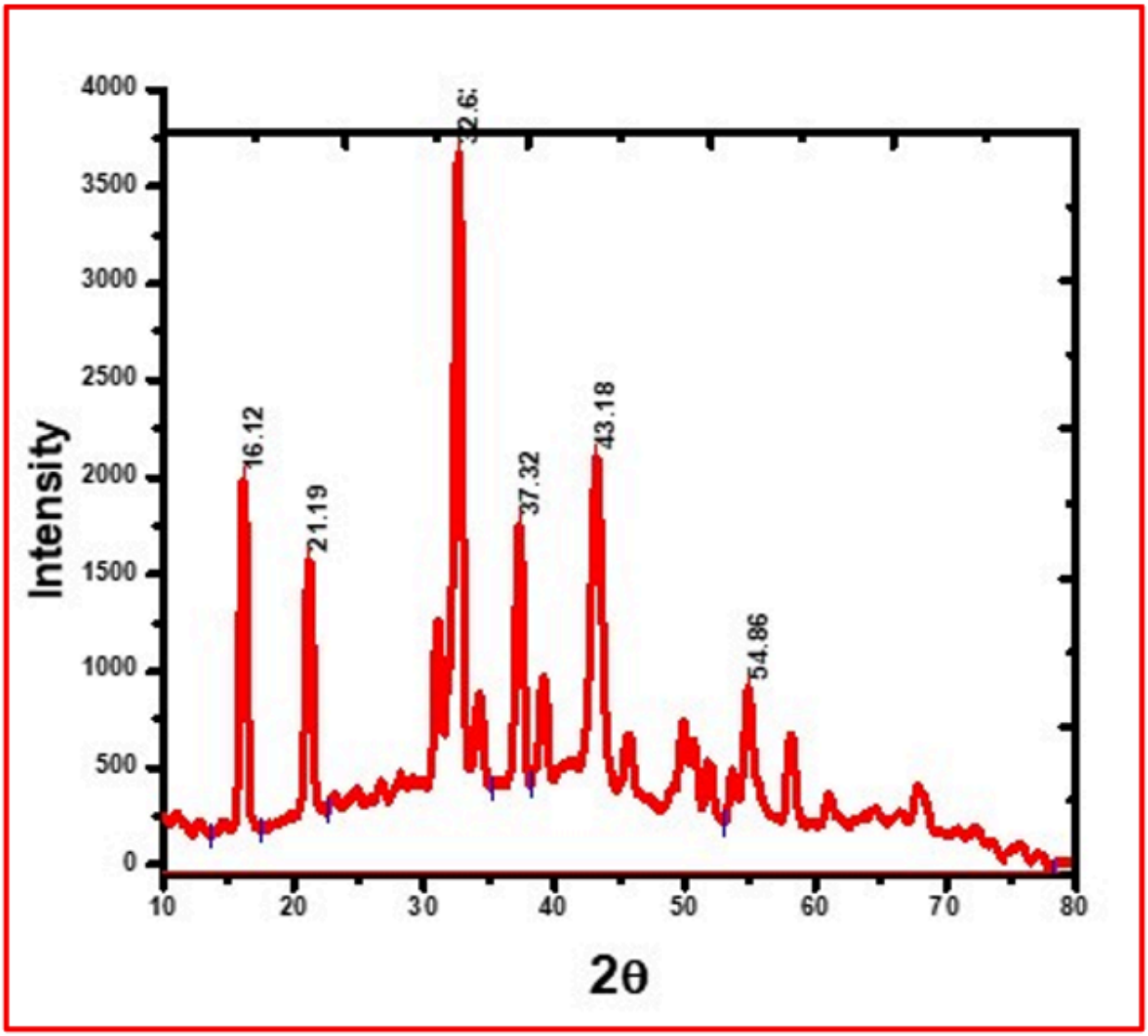

Figure 4

XRD spectrum of synthesized CO@FeNPs

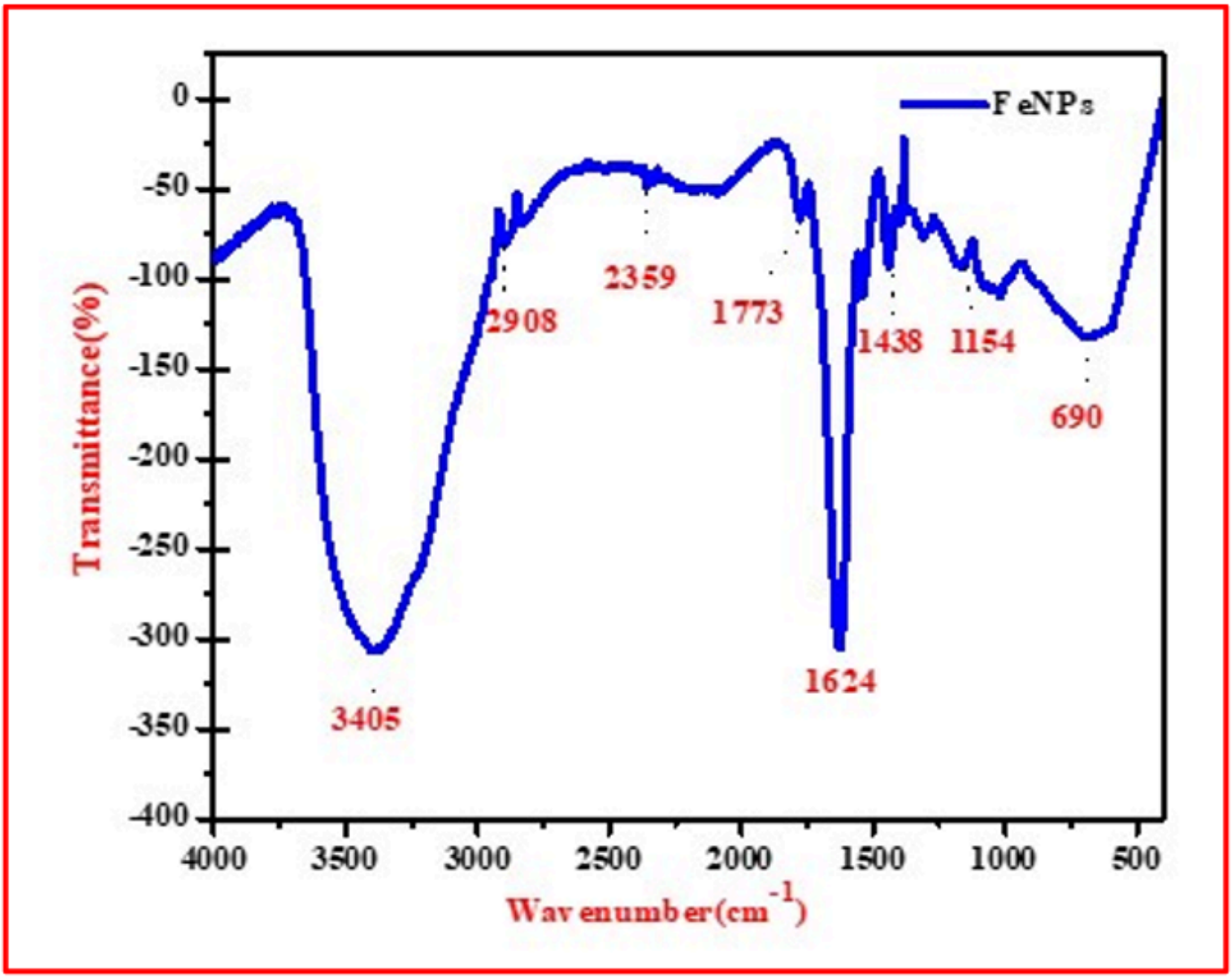

Figure 5

FTIR Spectrum of the prepared CO@FeNPs

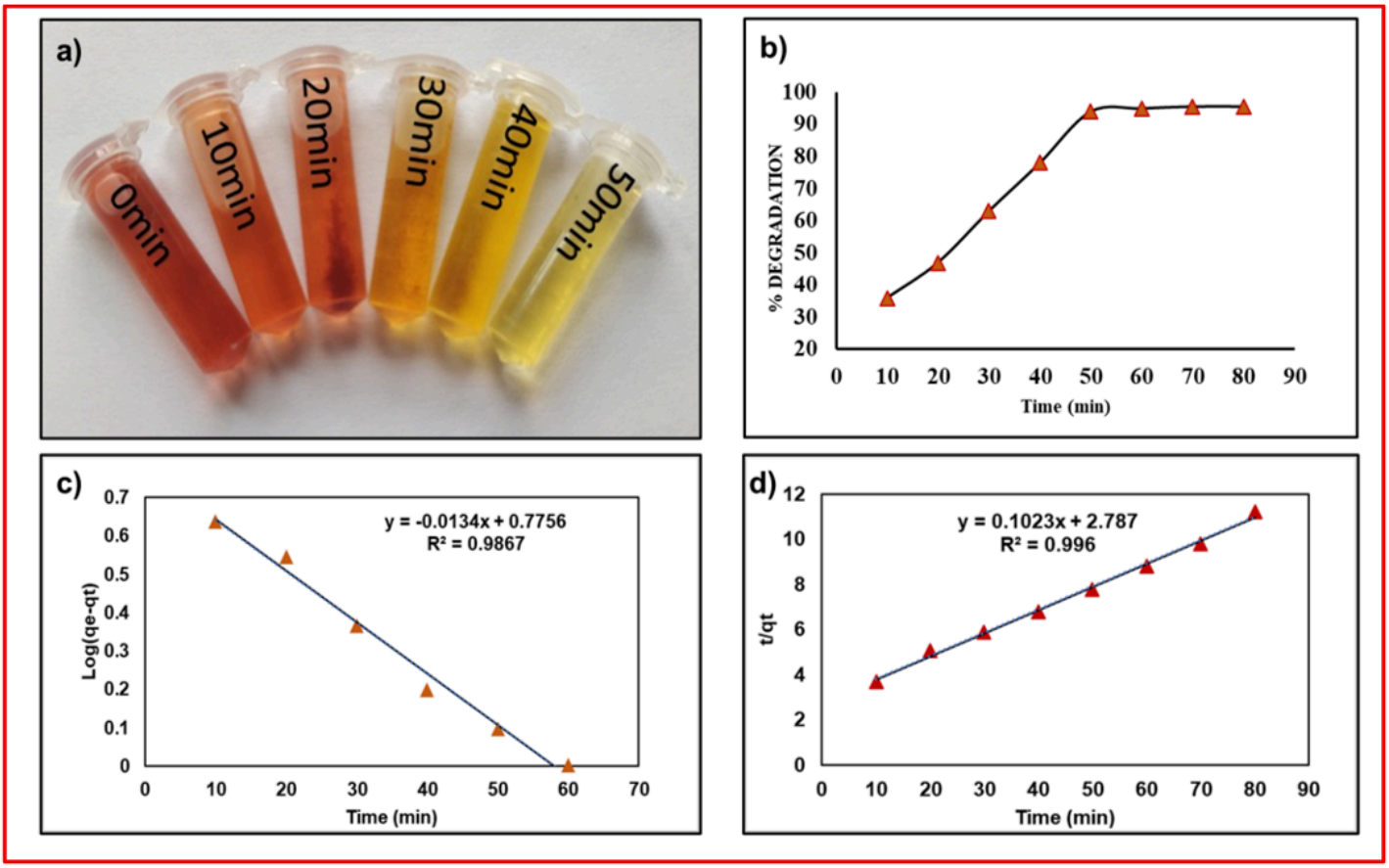

Figure 6

(a) Photographic images of time effect of photocatalytic degradation (b) Time-dependent study of MO by CO@FeNPs, (c) the pseudo-first-order, and (d) the pseudo-second-order

Figure 7

Photographic images of the effect of dye concentration

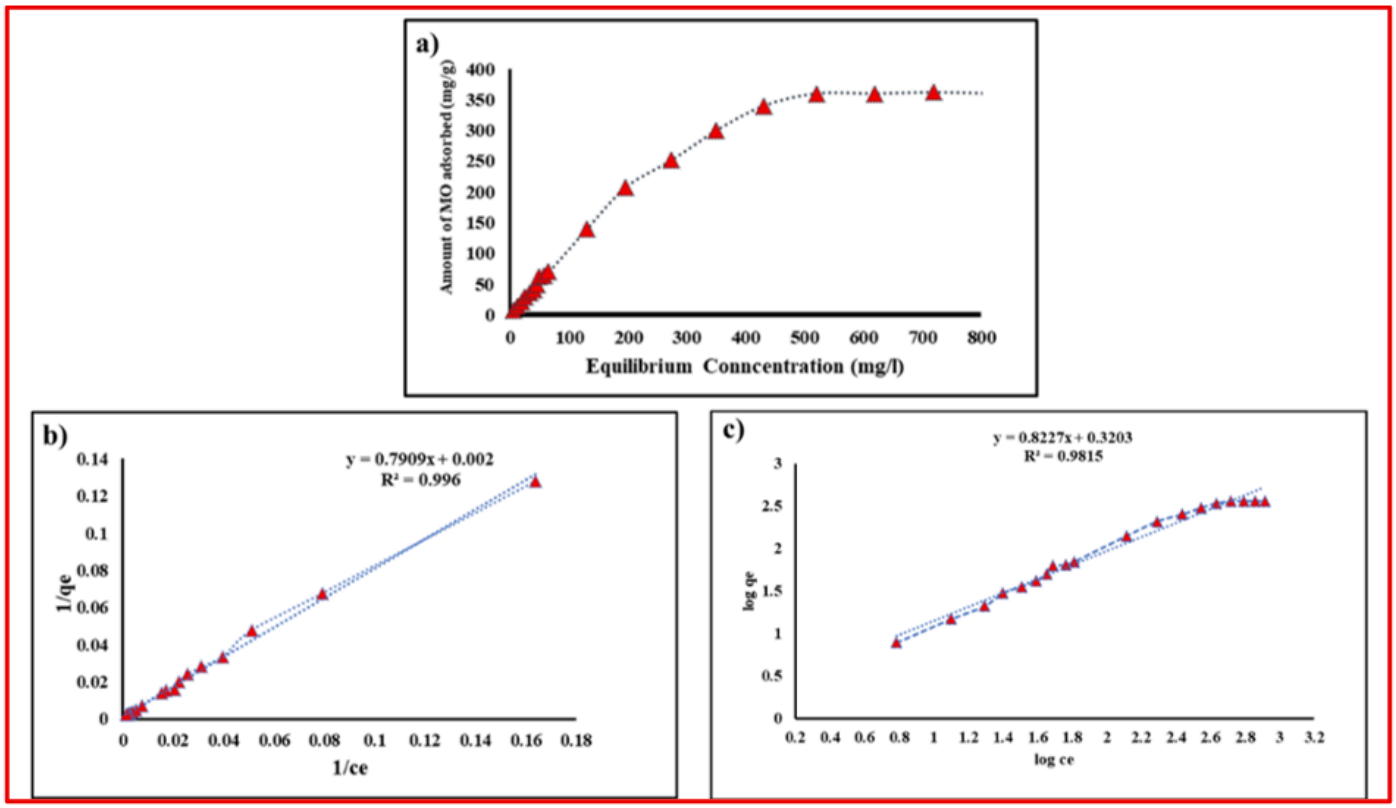

Figure 8

(a) Equilibrium sorption isotherm of MO (b) linearized langmuir plot (c) linearized freundlich plot.

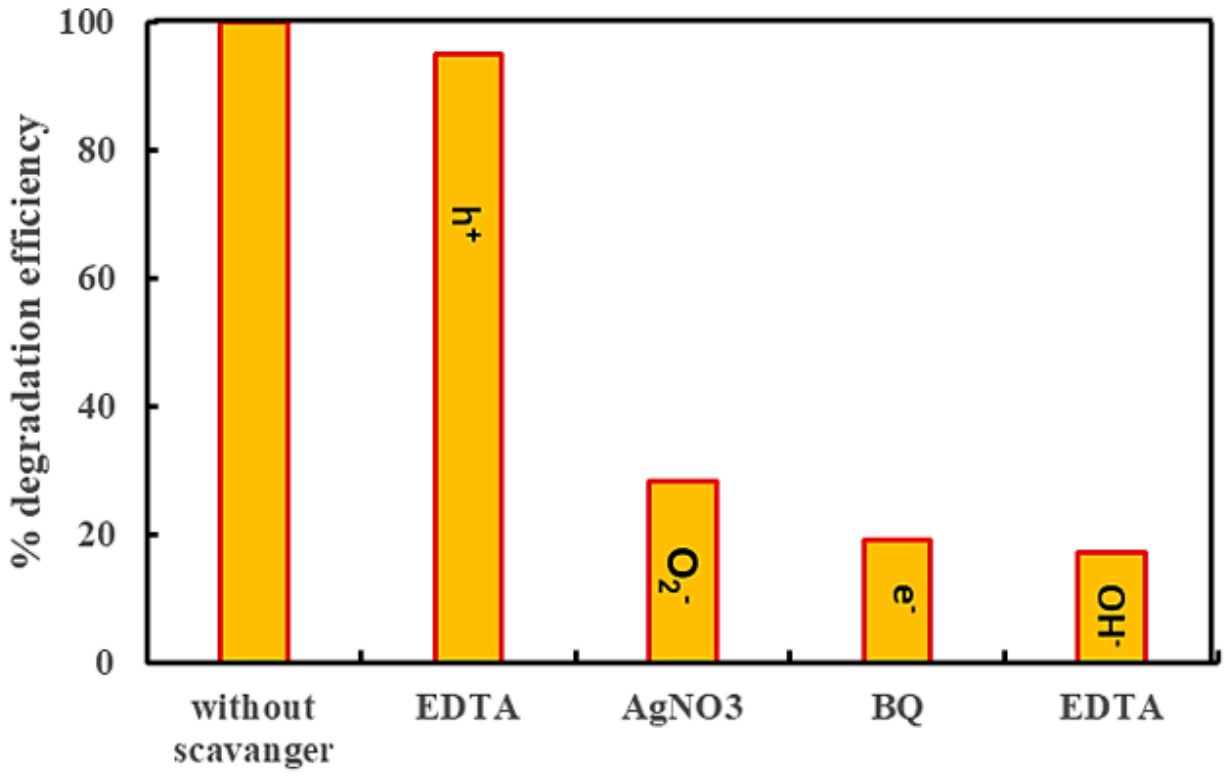

Figure 9

Scavenging study for the degradation of dyes

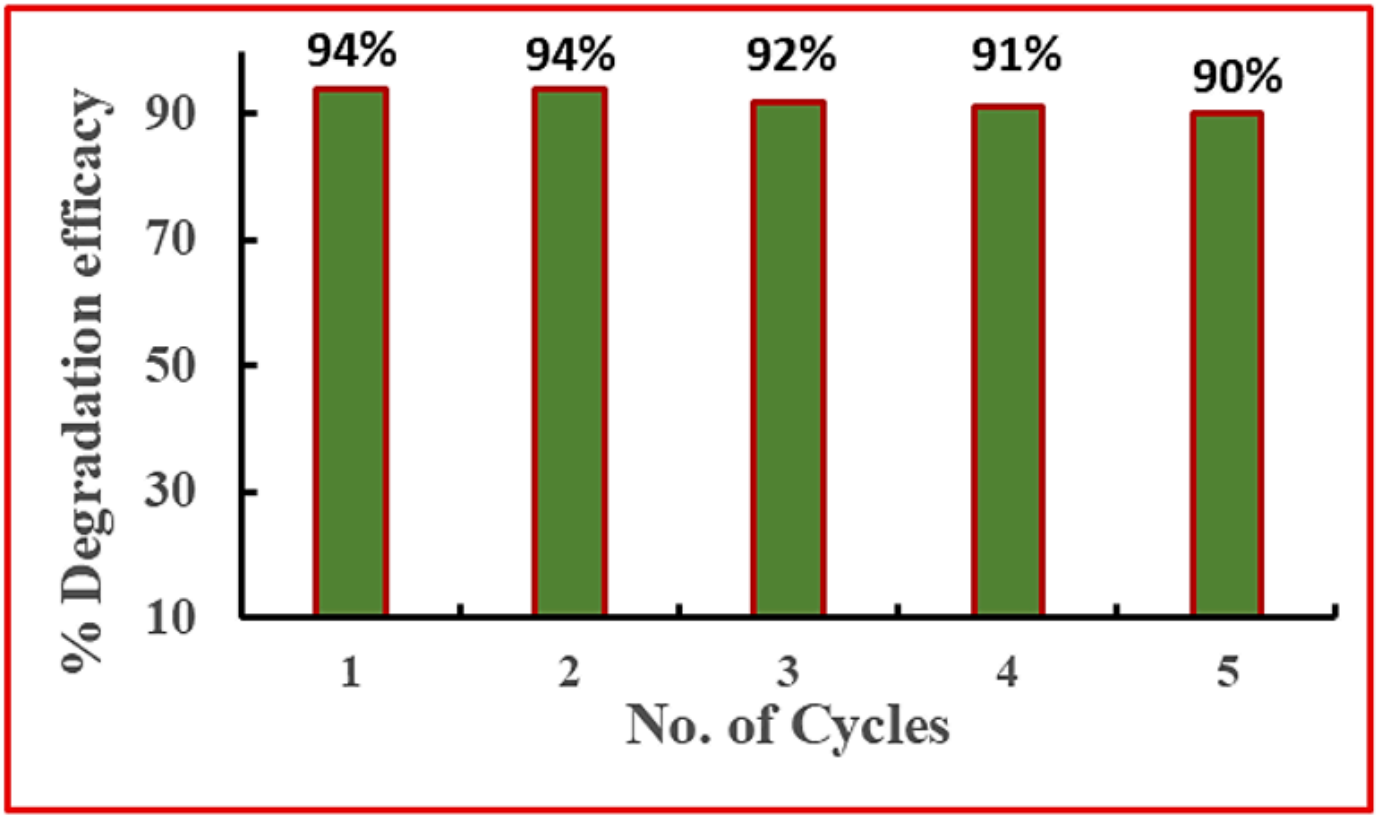

Figure 10

Reusability and photocatalytic stability for 5 runs

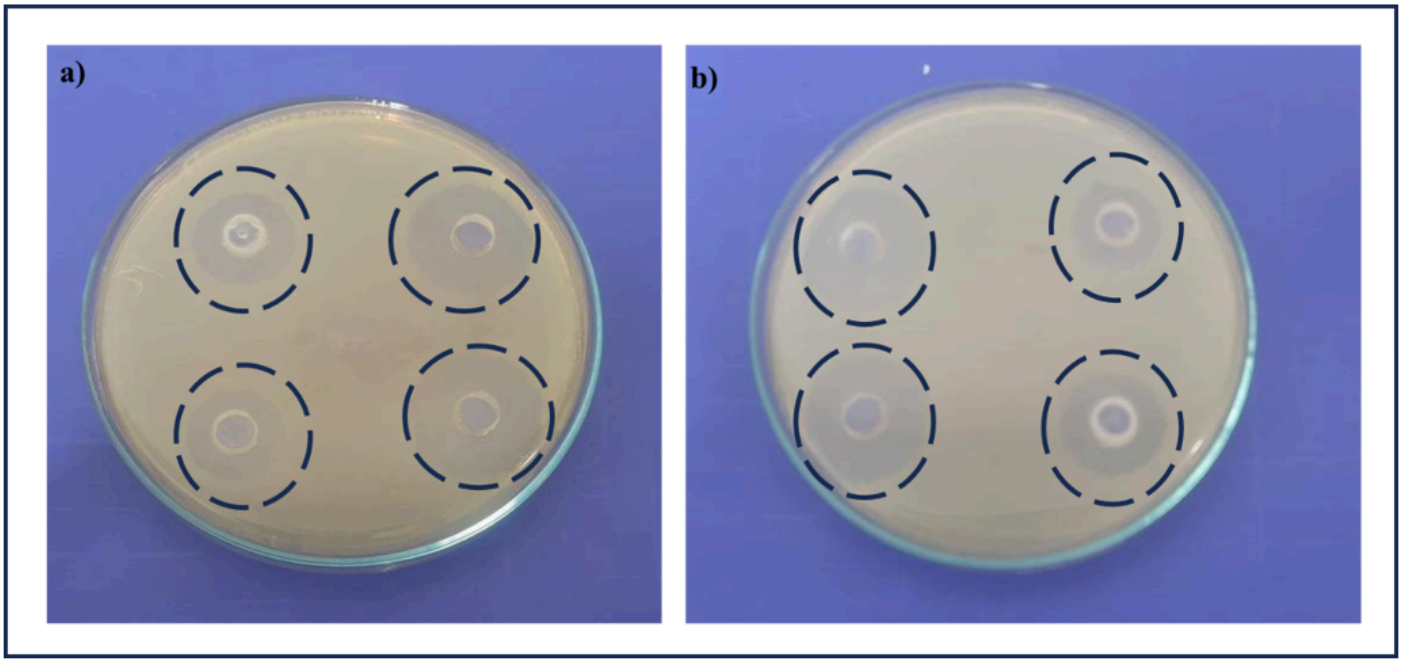

Figure 11

Pictorial representation of zone of inhibition of CO@FeNPs against a) *E. coli* and b) *S. aureus*

Supplementary Files

This is a list of supplementary files associated with this preprint. Click to download.

- Schemes.docx